# TESTING INTERFACES OF LATTICE SPACECRAFT STRUCTURES

**Brendan R. Murray [(1)], Kelly Matthews [(1)], Robert Telford [(1)]**

*[(1)] ATG Innovation Ltd., Office 11 & 12 Level One, Unit 8, Galway Technology Park, Galway, H91PX3V, Ireland. Email: brendan.murray@atg-europe.com*

## KEYWORDS

Composite, lattice structure, attachment, uninterrupted fibre-placement, cylinder, satellite central tube, interstages.

## ABSTRACT

A carbon fibre reinforced plastic (CFRP) lattice satellite central tube (SCT) demonstrator was designed to include various configurations of integrated laminate patches for typical SCT interface attachment points. An extensive breadboard test campaign of element level attachment samples based on these designs were then tested for in-plane, out-of-plane and bending loading configurations, to verify the structural integrity of the lattice attachment points. Samples assessed different design features with tests validating prediction methods on a local level before progressing to manufacture of the full-scale demonstrator. Test results showed that all interface requirements were met, with predicted failure loads exceeded for all attachment types (bar one), thus highlighting the overall conservatism in the current lattice design, modelling, and analysis methods. This successful testing allowed for progression to manufacturing of the demonstrator with confidence in the overall design's predicted behaviour.

## 1. INTRODUCTION

Lattice structures consist of a repeating grid pattern of intersecting stiffeners or ribs creating a mass optimised structural design. This architectural design concept has seen significant research with a renewed focus on composite materials due to the benefits of incorporating their unidirectional properties into lattice design concepts [1-8]. Composite lattice designs can provide potential mass savings of up to 30-50% in comparison to traditional design methods (sandwich, monolithic, etc), making them incredibly attractive for structural applications in large scale space components.

While lattice structures have seen significant research investment, the attachment methods by which the lattice interfaces with surrounding structures have not been as detailed. ATG Europe has undertaken research in developing design, manufacturing, and analysis methods for these attachment concepts [9-13] with the current work building on initial development programmes for attachments at element [12] and full-scale levels [13].

As part of an ESA Science Core Technology Programme (CTP), ATG Innovation Ltd. (a subsidiary of ATG Europe) designed a lattice SCT demonstrator which included various configurations of integrated laminate patches, providing attachment points for surrounding structures and equipment including shear panels, fuel tanks, radiator decks, payload decks, and payload module attachment points. The demonstrator also included an interface joint between the CFRP cylinder and an aluminium interface ring, which in turn provides an interface to a launch vehicle payload adaptor system.

One of the main aims of this CTP program was to prove that lattice structures can include integrated attachment points that can carry representative satellite interface loads. To this end, an extensive breadboard test campaign that encompassed various patch designs and configurations, was undertaken to provide comparisons to analytical predictions. Representative samples were also tested to validate the design and analysis methods used to assess the CFRP to aluminium interface joint. These tests were used to validate the methods developed to analyse attachment points in lattice structures with this paper giving an overview of the design, manufacturing, and testing of these samples with a review of results versus predictions.

## 2. METHODOLOGY

### 2.1. Lattice Structure Design Overview

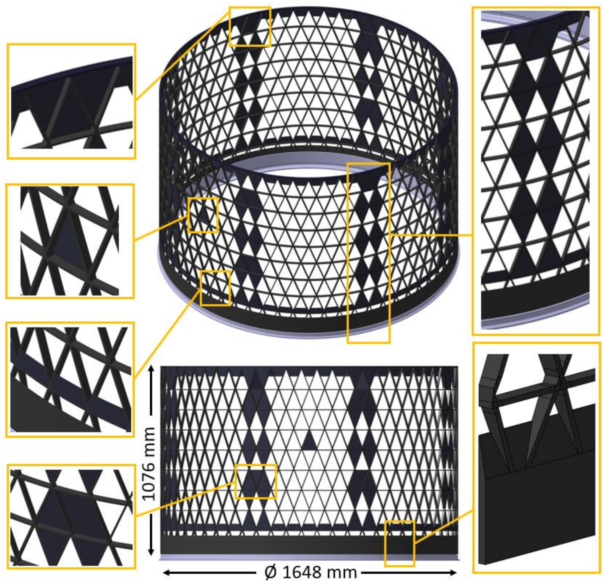


*Figure 1: Demonstrator lattice SCT with different features and attachment types highlighted.*

The demonstrator design consisted of a lattice SCT which was 1.644 m in diameter (OD) and 1.076 m in height, as shown in Fig. 1. The lattice part was made with Toray RS-36/M55J unidirectional prepreg with an aluminium PAS 1666S interface ring and weighed 36.7 kg in total. The composite structure alone weighed 26.7 kg (excluding the interface ring and insert masses). The ribs were 13.5 mm high by 4.4 mm wide with a helical angle of 21°. Several different attachment types were included in the design, with full and partial cell coverage, two patch thicknesses (2.145 mm and 7.02 mm), and two insert sizes (M6 and M10) used. All patches were quasi-isotropic layups. An Al 7075-T6 insert with a helicoil thread was bonded into a drilled hole in each patch to act as the attachment point. The end laminate was 7.02 mm thick and provides the connection to the PAS 1666S interface ring.

The demonstrator design followed that of a typical SCT which used representative loads to drive lattice design parameters. These loads were defined using ESA missions (specifically PLATO [14]), where equipment masses were assessed with gravitational accelerations from project requirements (-10g axial and +/-4.5g lateral). Additional load factors Kp and Km as defined in [15] were also applied. These loads were then distributed between the relevant attachment points in the design, according to a typical mass and payload configuration, to define requirement loads for the element level sample tests.

### 2.2. Sample Designs and Test Program Outline

The element level samples were designed to reflect the actual attachment designs in the SCT demonstrator while still maximising the information captured across the different patch types. Five different attachment designs (TA1 to TA5) were assessed for in-plane, out-of-plane and bending (TA1, TA2, and TA5 only) load cases with a further breakdown of the designs given in Tab. 1, along with an outline of the number of tests of each type completed. The TA5 specimens were re-used in all tests and so were only tested to 80% of the predicted failure load for each configuration. This 80% level was still above the interface requirement.

All samples reflected the demonstrator lattice design parameters (rib sizes, angles, and manufacturing parameters) but were made using a flat lattice grid to produce multiple samples in a single production run while also facilitating simpler test set-ups. Samples were cut from the flat lattice panel and then embedded in a potting material to allow for constraint in the relevant test fixtures.

An additional assessment of the interface region design, which consists of a hybrid bonded and fastened joint, was conducted using a standard bolted lap shear specimen based on ASTM D5961 and a more complex element level sample (TIF1 to TIF3), which mimicked the interface joint design more closely. These samples were tested in compression, with design details provided in Tab. 2 along with a further breakdown of the number of tests conducted. 10 thermal vacuum cycles and 90 thermal cycles (in nitrogen) were also conducted on the TIF2 and TIF3 samples before compression testing. This was undertaken to assess environmental effects (like those expected during operation) on the joint designs as there were high CTE differences between the dissimilar materials (composite, adhesive, and metal).

*Table 1: Attachment test specimen overview.*

| ID | Design | Details | IP | OOP | Bending |
|---|---|---|---|---|---|
| TA1 | 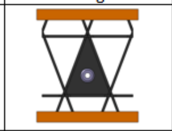 | Patch T : 7.02 mm<br>Insert : M10 | 7 | 7 | 7 |
| TA2 | 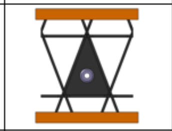 | Patch T : 2.145 mm<br>Insert : M10 | 7 | 7 | 7 |
| TA3 | 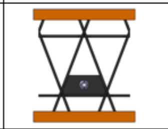 | Patch T : 2.145 mm<br>Insert : M6 | 7 | 7 | - |
| TA4 | 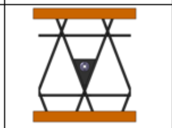 | Patch T : 2.145 mm<br>Insert : M6 | 7 | 7 | - |
| TA5 | 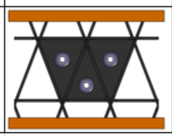 | Patch T : 7.02 mm<br>Insert : M10 x 3 | 4 | 4 | 4 |

*Table 2: Interface joint element level test samples.*

| ID | Design | Details | Compression |
|---|---|---|---|
| TIF1 |  | ASTM D5961<br>1/4 Inch Hi-Lite x 2 | 7 |
| TIF2 | | ASTM D5961<br>1/4 Inch Hi-Lite x 2<br>100 Thermal Cycles<br>(+100°C to -70°C) | 7 |
| TIF3 | 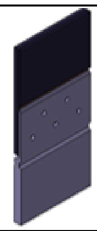 | 1/4 Inch Hi-Lite x 5<br>100 Thermal Cycles<br>(+100°C to -70°C) | 5 |

### 2.3. Finite Element Modelling

All samples were analysed using FEMAP with NX Nastran. Models used solid laminate elements with layup definitions defined using PCOMP properties. Loads were applied using a node at the centre of the insert which was connected to the inner insert surface using an RBE2 as shown in Fig. 2. The IP loads were applied in the -Z direction, the OOP loads were applied in the +X direction, and the bending moment was applied about the +Y direction (all in relation to Fig. 2). The bending load cases used an offset distance of 220 mm from the insert front face to apply the desired load/moment. The TA5 specimens, which utilised a multi-cell patch configuration, featured an additional RBE2 to connect the three attachment points together. Boundary constraints for each load case were applied to the potting directly while constraints on the loading node mimicked that of the applied load in the test fixtures.

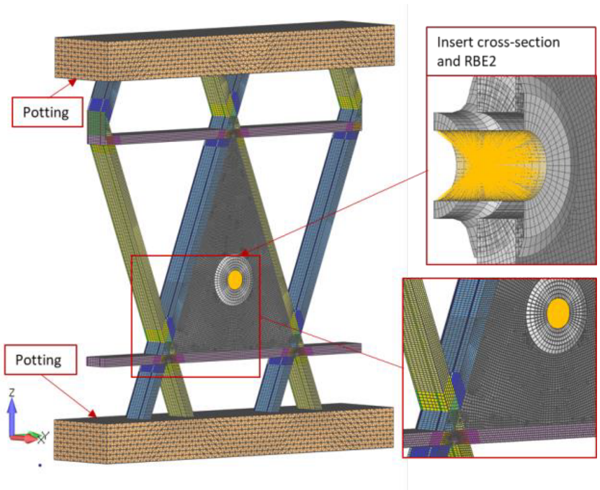


*Figure 2 Overview of finite element model with the insert RBE2 highlighted.*

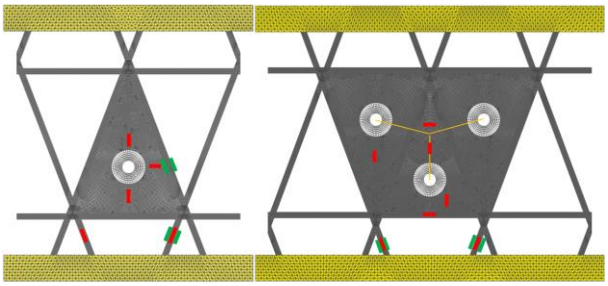

*Figure 3: Typical strain gauge locations (red = front and back faces, green = along rib thickness).*

For correlation to test results, representative strain gauges were implemented in the FE model at corresponding locations to the test samples using low stiffness compliant rod elements, with an overview of typical strain gauge locations given in Fig. 3. Failure indices were calculated using a maximum strain failure criterion, using average strain allowables obtained from coupon level tests from previous projects. All FE analysis images shown hereafter are from post-correlation assessments and show the measured failure load against the corresponding failure index prediction.

### 2.4. Sample Testing

The goal of the element level tests was to exceed the defined requirement loads while also achieving representative failure loads and locations which were in line with those predicted.

#### *2.4.1. Test Fixtures*

For the TA attachment tests, three different test rigs were used to apply IP, OOP and bending loads with overviews of these designs given in Fig. 4. Samples were constrained by plates which allowed sliding along the front and back faces of the sample potting, and by blocks which acted as reaction points for the top and bottom faces of the sample potting, in a manner which mimicked the boundary conditions applied in the FEA assessments.

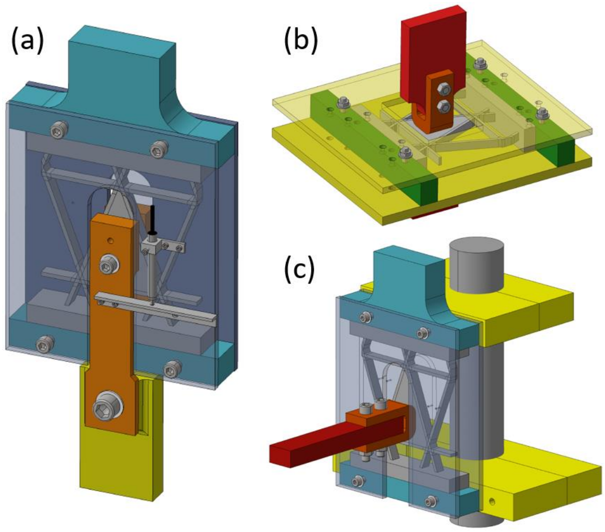


*Figure 4: Overview of attachment test fixtures for (a) IP, (b) OOP and (c) bending load cases (with transparent front plates to see sample locations).*

Standard grips were used to clamp the TIF samples in a compression test machine which applied the required load for the specimens. Tests followed ASTM D5961 where applicable, with modifications to the TIF3 testing due to the non-standard sample design. All tests were run in displacement control.

#### *2.4.2. Strain gauges and LVDTs*

Strain gauges were applied in locations as outlined in Fig. 3 already, while LVDTs were used to measure load fixture arm movement and sample displacements (where possible due to the encompassing fixtures) at points which were mapped back to the FEA undertaken previously as outlined in section 2.3.

#### *2.4.3. Digital Image Correlation (DIC)*

DIC was used for the TA5 bending tests and TIF3 compression tests as these were the only samples with visible surfaces during testing. DIC is an optical, non-contact measurement technique which tracks discrepancies in a series of images over time to measure surface displacements and strains. The camera system used was a LaVision 3D DIC setup. Images were captured at a frequency of 1 Hz. DaVis

8.4.0 StrainMaster software from LaVision was used to post process all images.

## 3. RESULTS

### 3.1. Attachment In-Plane

All attachment types (TA1-TA5) were subjected to IP testing. An overview of the predicted and measured results is given in Tab. 3. Some initial damage events (non-linearity) were seen during testing, but these did not affect the overall stiffness of the samples and so tests were continued to ultimate failure. The ultimate failure load exceeded that of the FEA predictions and requirements for all samples.

*Table 3: Predicted and measured IP test results.*

| Test | Predicted Failure Load (N) | Average Ultimate Failure Load (N) |
|---|---|---|
| TA1 | 22340 | 45666 |
| TA2 | 14415 | 21392 |
| TA3 | 6915 | 12587 |
| TA4 | 10805 | 10961 |
| TA5 | 47270 | * |

For the TA1 samples, FE analyses showed that the area of highest failure index (FI) would be in the helicals just below the bottom hoop rib, with mechanical testing proving this accurate as shown by the failure image in Fig. 5. Micro sectioning of the sample post testing showed no other failures were present.

While the TA2 sample is similar to the TA1 sample, the relative patch thickness plays a significant role in the load bearing capacity of the sample. As such, the thinner TA2 patch had a higher predicted FI in t area around the insert, as shown by Fig. 6, with bearing failure noted around the insert in the actual test.

For the TA3 samples, the partial patch sees significant load ingress into the free edge at the top of the patch as the IP load is applied. The FEA shows the area of highest FI is in this region, with high FIs horizontal to the inserts midplane position. Physical testing mirrored these failure mechanisms with both present as shown by Fig. 7.

For the TA4 specimen, the design shape forces the applied IP load to funnel into the patch tip and node region, which induces a high FI as shown by Fig. 8. High FIs were also present in the region just below the insert at the rear surface of the patch via bearing failure. These predictions were proven to be an accurate assessment via visual and microscopic inspections.

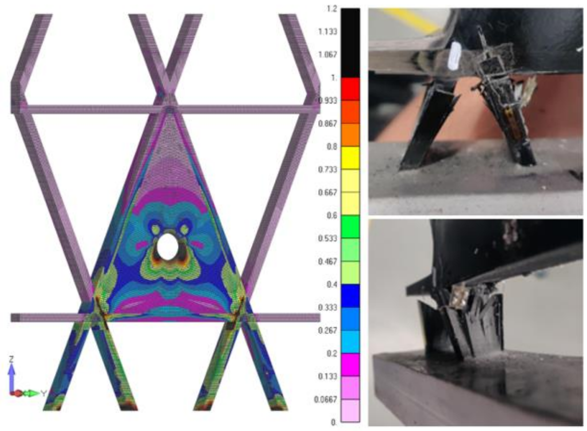

*Figure 5: FI contour plot of the front surface of the TA1 IP test with an image of the leg failures.*

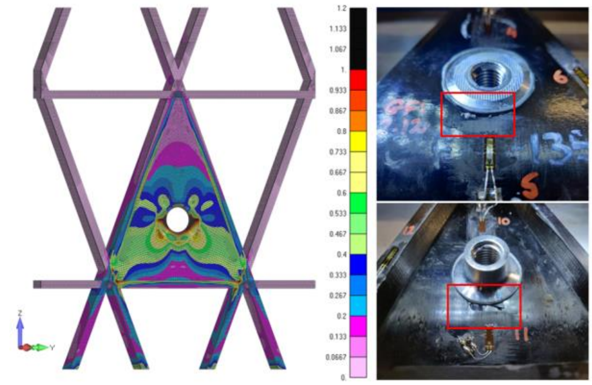

*Figure 6: FI contour plots of the front surface of the TA2 IP test with an image of the patch failure.*

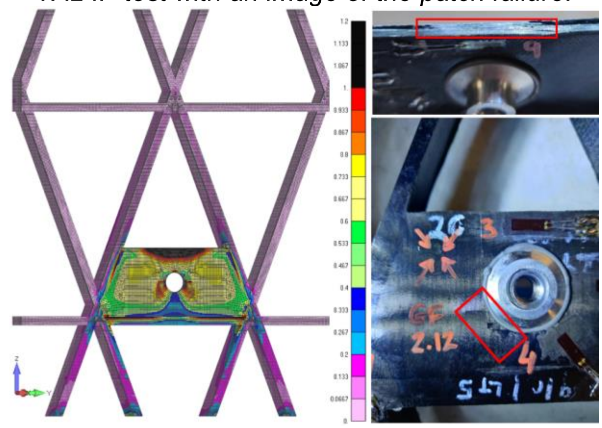

*Figure 7: FI contour plots of the front surface of the TA3 IP test with an image of the patch failure.*

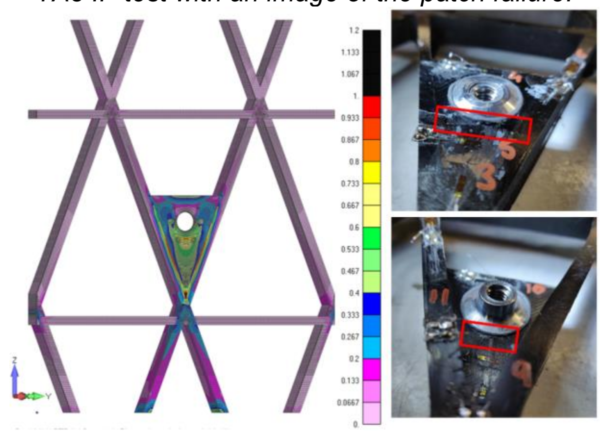

*Figure 8: FI contour plots of the front surface of the TA4 IP test with an image of the patch failure.*

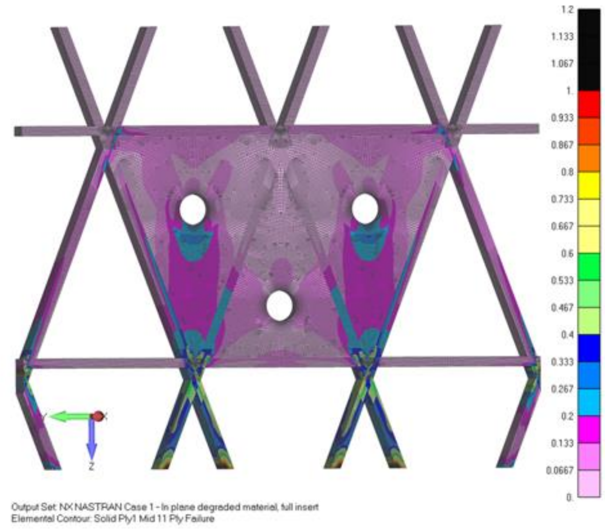


*Figure 9: FI contour plot of the of the front surface of the TA5 IP test.*

While the TA5 specimens were not tested to failure (as they were re-used in all tests), the predicted failure location was in the helical legs just below the patch as shown in Fig. 9, in a similar manner to the TA1 samples. The TA5 samples did not show any failure characteristics when tested to 80% of the predicted failure load, and measured strains followed predicted strains in a consistent manner with no failure events recorded.

As mentioned, some initial failure mechanisms (non-linearities) were noted across all tests, but these events were non-critical occurrences as they had limited impact on the overall stiffness behaviour and did not lead to an appreciable drop in the load bearing capacity of the samples.

### 3.2. Attachment Out-of-Plane

*Table 4: Predicted and measured OOP test results.*

| Test | Predicted Failure Load(N) | Average Ultimate Failure Load (N) |
|---|---|---|
| TA1 | 5455 | 9040 |
| TA2 | 1695 | 1750 |
| TA3 | 1005 | 1353 |
| TA4 | 1665 | 1264 |
| TA5 | 7600 | * |

All attachment types (TA1-TA5) were subjected to OOP testing. An overview of the predicted and measured results is given in Tab. 4. The ultimate failure loads exceeded that of the FEA predictions for all samples except TA4, which failed at a lower load level than predicted, with analyses showing good failure location correlation overall. Some initial failures below predictions were also present but these did not affect the overall stiffness of the samples and so tests were continued until ultimate failure.

For the TA1 samples the OOP test results exceeded predictions, and failure was in the surrounding ribs as predicted. From Fig. 10, the expected failure location was in the intersection between the helical and hoop rib which propagated into the rest of the helical as shown by the failure images included.

The TA2 samples followed a similar trend with average sample failure loads exceeding predictions for OOP tests, with high FI locations consistent with observed failure locations. As shown in Fig. 11, the highest failure indices were in the helical and hoop ribs surrounding the patch, and in the area surrounding the insert. The tested TA2 samples showed failures in the ribs as predicted, with the area surrounding the insert having no visible damage (though this had a lower predicted FI in comparison).

For the TA3 samples all requirements and predictions for OOP tests were exceeded, with highest FIs predicted in the lower hoop rib to patch connection, and FI>1 in the helical to patch connection and in the area around the insert as shown in Fig. 12. From the actual test results, failure in the hoop and helical to patch interface points was captured, but no damage in the area surrounding the insert was visible in a similar manner to the TA2 samples (again where lower FIs were present).

For the TA4 samples, while the interface requirements were met, the ultimate failure load was under that predicted by the FEA while failure locations were consistent with predictions. From Fig. 13 the highest FIs were in the region surrounding the insert and at the helical patch connection interface. From tested samples, the visible failure was in the helical-patch transition with no subsequent damage found around the insert. It's possible that the close nature of the failure indices (at 1.01 to 1.04) means failure could occur in either point quite easily with the release of strains effecting the follow-on failure mechanisms around the insert.

For the TA5 samples, while not tested to failure, failure was predicted to occur in the helical legs below the bottom hoop rib. However, the TA5 samples did not show any failure characteristics when tested to 80% of the predicted failure load, and measured strains followed the predicted strains in a consistent manner with no failure events recorded.

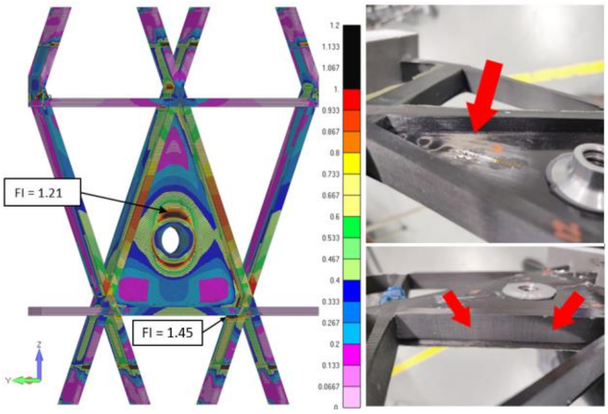


*Figure 10: FI contour plots of the rear surface of the TA1 OOP test with images of failure.*

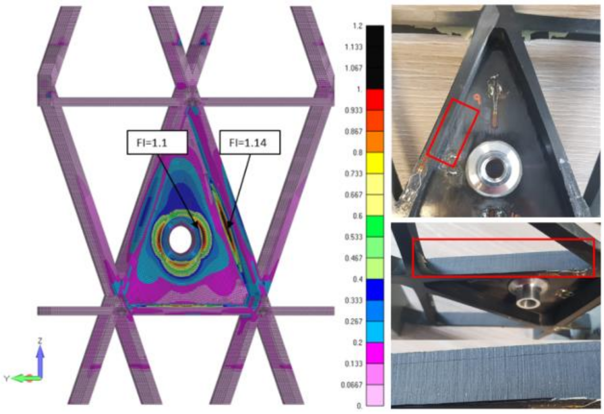


*Figure 11: FI contour plots of the rear surface of the TA2 OOP test with images of actual failures.*

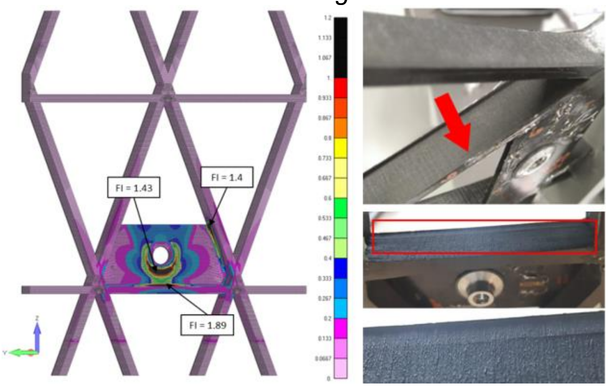


*Figure 12: FI contour plots of the rear surface of the TA3 OOP test with images of actual failures.*

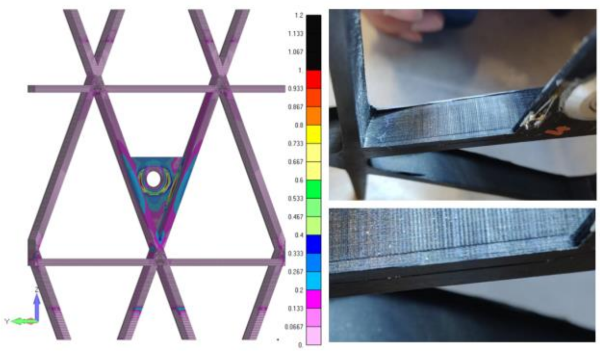

*Figure 13: FI contour plots of the rear surface of the TA4 OOP test with images of actual failures.*

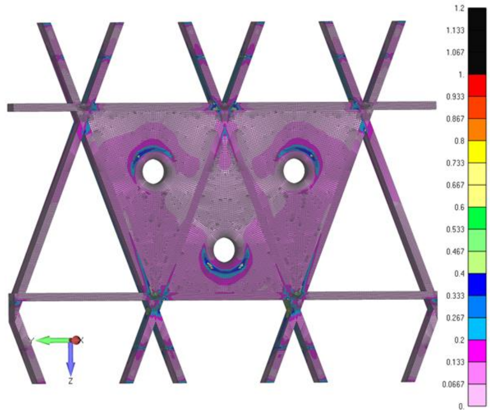

*Figure 14: FI contour plots of the front surface of the TA5 OOP test.*

### 3.3. Attachment Bending

Only the TA1, TA2 and TA5 samples were subjected to bending tests as the partial patch designs (TA3/TA4) are not designed to take these more complex loads. The TA5 bending test was not run to failure, instead they were tested to 347 Nm (80% of the predicted failure load) as the samples were used over multiple tests as previously discussed. An overview of all results is included in Tab. 5. The ultimate failure load for all samples exceeded that of the FE predictions in all cases.

*Table 5: Predicted and measured bending results.*

| Test | Predicted Failure Load (Nm) | Average Ultimate Failure Load (Nm) |
|---|---|---|
| TA1 | 132 | 234.7 |
| TA2 | 27.5 | 66.2 |
| TA5 | 433 | * |

For the TA1 and TA2 samples, the FI peaks were highest in the areas just above the top insert edge and in the helical ribs adjacent to this point as shown by Fig. 15 and Fig. 16 respectively. Results from physical tests showed failures in the same locations for both samples as shown via microscopy and the images provided.

For the TA5 specimens (while not tested to failure), the predicted failure location was under the bottom most insert as shown in Fig. 17. The samples did not show any failure characteristics when tested to 80% of the predicted failure load, and measured strains followed the predicted strains in a consistent manner. DIC analyses also confirmed that the area of highest strain was just below the insert (seen in Fig. 18), with DIC measured surface strains matching the measured strain gauges in a similar manner giving further confidence in the finite element predictions.

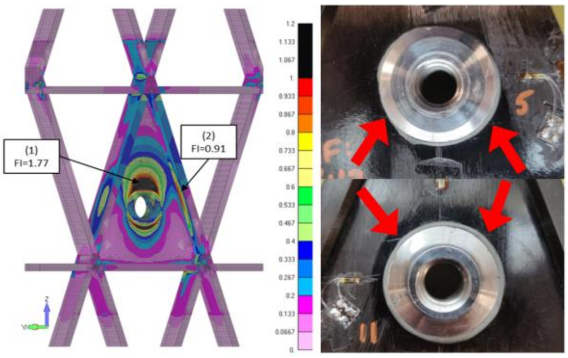


*Figure 15: FI contour plots of the rear surface of the TA1 bending test with images of failures.*

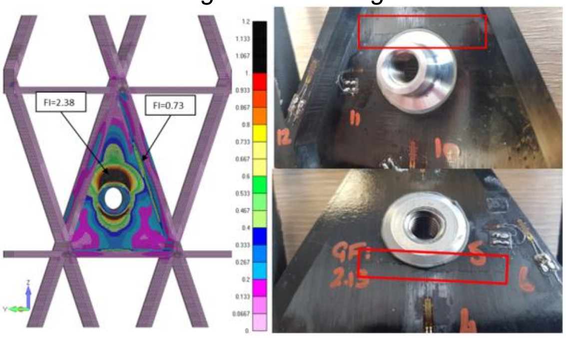


*Figure 16: FI contour plots of the rear surface of the TA2 bending test with images of actual failures.*

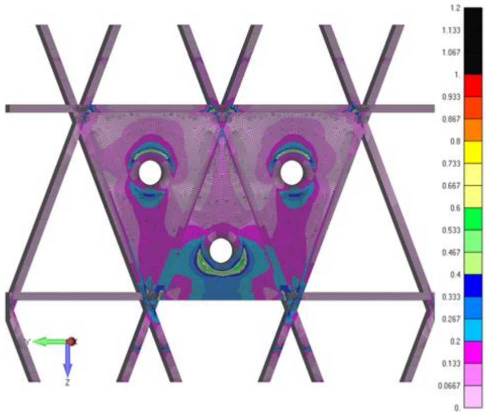

*Figure 17: FI contour plot of the of the rear surface of the TA5 bending test sample.*

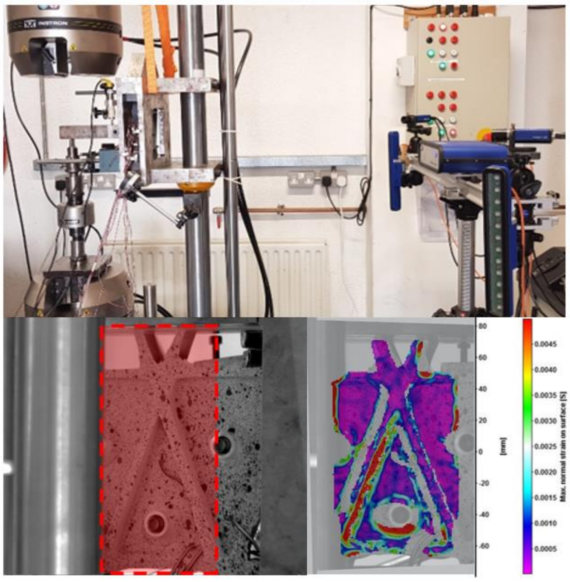

*Figure 18 DIC setup for the TA5 bending test showing the field of view and strain output map.*

### 3.4. Interface Samples

For the interface samples, the TIF1-2 samples were used as a standardised test for the materials being used in the interface joint design. No FEA predictions were made for these tests. Results showed differences in the responses between the TIF1 and (thermally cycled) TIF2 samples, with the TIF1 samples having a higher initial stiffness but a similar load progression thereafter. This was most likely due to the thermal cycling which caused bond degradation in the interface region between the composite and metal surfaces of the TIF2 samples, which was proven by C-scanning of post cycled samples prior to testing, reducing their initial stiffness. However, the maximum bearing stress for both sets of samples was approximately equal to 575 MPa, showing that both have similar ultimate failure capacity where the fasteners are taking the majority of the load.

The FEA predictions for the TIF3 samples showed failure occurring in the composite section of the sample through bearing failure in the upper row of fastener holes and just above the end of the interface with the aluminium section at a compressive load of 30 kN (with Fig. 19 showing this at the actual failure load level of 79.9 kN). This failure location proved to be accurate as the sample failed in the same region, as shown in Fig. 20, but with an average ultimate failure load of 79.9 kN.

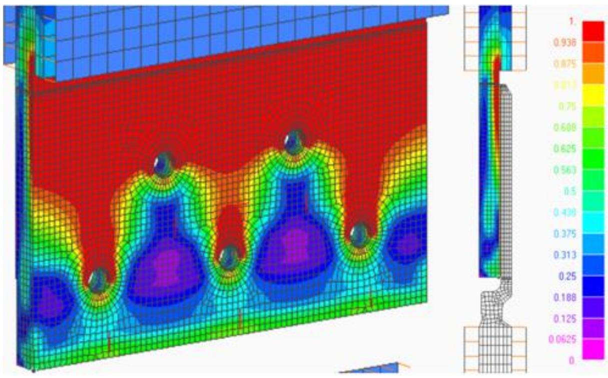

*Figure 19: Compressive failure in TIF3 samples at 79.9 kN.*

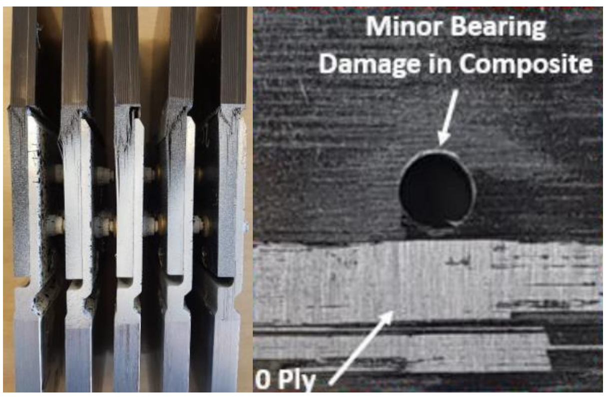


*Figure 20: Failure in TIF3 samples.*

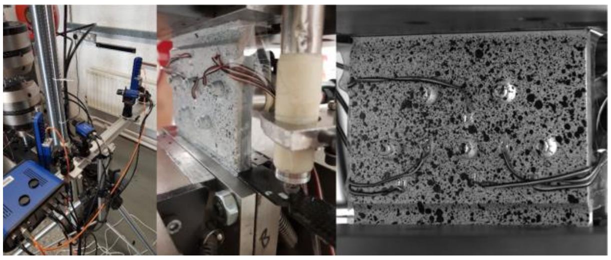

Figure 21: DIC setup for the TIF3 test specimens.

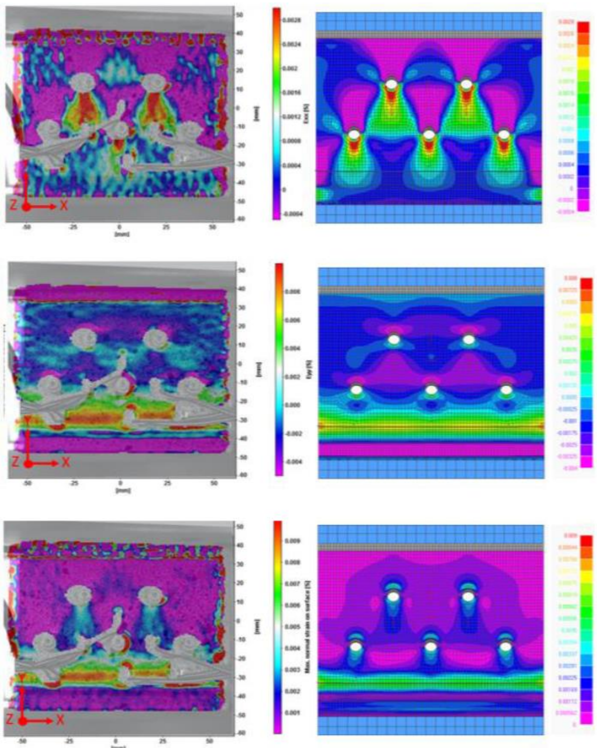

Figure 22: DIC measured strains versus FEA predictions.

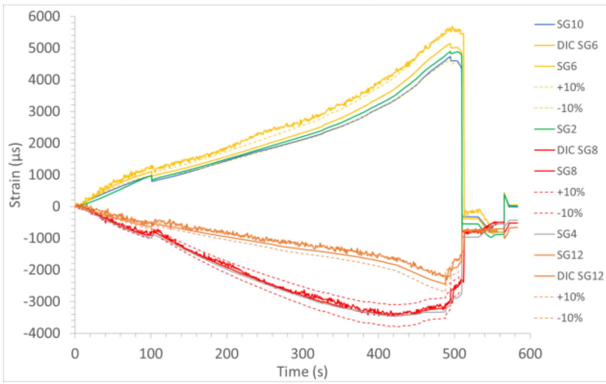


Figure 23: DIC measured strains versus strain gauge readings for a TIF3 test.

There was an initial small load drop in the samples at the lower load level of 30 kN but this was most likely from the bond degradation of the joint via thermal cycling (similar to the TIF2 samples), which was also confirmed by C-scan imaging post thermal cycling and prior to mechanical testing, and via assessments of the failed samples post-testing.

DIC was also used to assess these samples during testing with the test setup shown in Fig. 21. From comparisons of predictions versus the full field DIC measurements (Fig. 22), and from a comparison of physically measured strains versus DIC measured strains (Fig. 23), good correlation to the finite element model was achieved.

These results equated to a maximum line load of 702 kN/m at ultimate failure with the initial or first failure equating to a line load of 264 kN/m. This is well in excess of the design requirement of 175 kN/m.

## 4. CONCLUSIONS

A representative lattice SCT was designed based on requirements from ESA specific missions. Element level samples, which reflected attachment points in this design, were mechanically tested with results showing all required loads were exceeded for design requirements. In addition, conservative correlations to finite element analyses for IP, OOP and bending load configurations were achieved for all sample types (except TA4 OOP) with predicted failure locations being consistent with actual failure results in all cases. This validated the current design and analysis methods developed for lattice structure attachment point designs. Furthermore, predictions for the interface ring joint samples also showed good correlation to the test results giving confidence in all assessments and allowing for progression to the manufacturing of the SCT demonstrator.

## 5. ACKNOWLEDGEMENTS

The authors would like to acknowledge the funding and support provided by the European Space Agency and Enterprise Ireland under the Science Core Technology Programme (CTP), without whom this project would not have been possible. They would also like to thank the manufacturing and testing teams at ÉireComposites Teo., led by Brandon Crosbie, as well as the ESA Technical Officer responsible for this project, Arnoud Keereman. This highly collaborative project would not have succeeded without the effort and dedication of all involved.

## 6. HEADERS AND FOOTERS

1. Huybrechts, S., Hahn, S., Meink, T. (1999) Grid stiffened structures: a survey of fabrication, analysis, and design methods. *12th Int Conf Compos Mater*. 1–10.
2. Totaro, G., De Nicola, F. (2012). Recent advance on design and manufacturing of composite anisogrid structures for space launchers. *Acta Astronaut.* (81), 570–7.
3. Chen, H., Tsai, S.W. (1996). Analysis and Optimum Design of Composite Grid Structures. *J. Compos. Mater*. 30(4), 503-534
4. Vasiliev, V.V, Barynin, V.A., Razin, A.F. (2011). Anisogrid composite lattice structures – Development and aerospace applications. *Compos. Struct.* (94), 1117-1127.

5. Lane, S.A., Kennedy, S., Richard, R. (2007). Noise Transmission Studies of an Advanced Grid-Stiffened Composite Fairing. *J Spacecr Rockets*. 44(5), 1131-1139
6. Zallo, A., Ippati, L., Grilli, A., De Nicola, F., Totaro, G., Giusto, G., Spena, P., Di Caprio, F., Mespoulet, S. (2019). Composite Grid Technology Applied to VEGA-C Interstage 2/3. *8th European Conference for Aeronautics and Space Sciences* (EUCASS)
7. Sanford, G.A., Higgins, J.E., Welsh, J.S. (2003). Advanced iso-grid fairing qualification test for minotaur launch vehicle. *14th Int. Conf. Comp. Mater.* San Diego, USA, 2003.
8. Bakhvalov, Y.O., Petrokovskiy, S.A., Polynovskiy, V.P., Razin, A.F. (2009). Composite irregular lattice shells designing for space applications. *17th Int. Conf. Comp. Mater.* Edinburgh, UK, 2009.
9. Pavlov, L., Te Kloeze, I., Smeets, B.J.R., Simionian, S.M. (2016). Development of mass and cost-efficient grid-stiffened and lattice structures for space applications. *14th Eur. Conf. Spacecr. Struct. Mater. Environ. Test.* Toulouse, France. 1149–1151.
10. Maes, V.K., Pavlov, L., Simonian, S.M. (2019) An efficient semi-automated optimisation approach for (grid-stiffened) composite structures: Application to Ariane 6 Interstage. *Compos Struct.* (209) 1042–1049.
11. Pavlov, L., Te Kloeze, I., Smeets, B.J.R., Simonian, S.M. (2017). WO2017099585A1: Composite Grid Structure Patent.
12. Smeets, B.J.R., Pavlov, L., Kassapoglou, C. (2016). Development and testing of equipment attachment zones for lattice and grid-stiffened composite structures. *14th Eur. Conf. Spacecr. Struct. Mater. Environ. Test.*, Toulouse, France.
13. Smeets, B.J.R., Fagan, E.M., Matthews, K., Telford, R., Murray, B.R., Pavlov, P., Weafer, B., Mieir, P., Goggins, J. Structural testing of a shear web attachment point on a composite lattice cylinder for aerospace applications. *Compos. B. Eng.* (212) 108691.
14. European Space Agency. (2017). PLATO - Revealing habitable worlds around solar-like stars. Definition Study Report. ESA-SCI(2017)1.
15. European Space Agency. (2019) Structural factors of safety for spaceflight hardware. ECSS-E-ST-32-10C.